AIP Advances

A simple two-step strategy to synthesize defect-rich MoS_2 nanocrystals for enhanced electrochemical hydrogen evolution

Cite as: AIP Advances **12**, 035119 (2022); https://doi.org/10.1063/5.0083934
Submitted: 31 December 2021 • Accepted: 12 February 2022 • Published Online: 10 March 2022

Dhirendra Sahoo, Jyoti Shakya, Sudipta Choudhry, et al.

A simple two-step strategy to synthesize defect-rich MoS_2 nanocrystals for enhanced electrochemical hydrogen evolution

Cite as: AIP Advances 12, 035119 (2022); doi: 10.1063/5.0083934
Submitted: 31 December 2021 • Accepted: 12 February 2022 •
Published Online: 10 March 2022

View Online Export Citation CrossMark

Dhirendra Sahoo,[1] Jyoti Shakya,[2] Sudipta Choudhry,[1] Budhi Singh,[3a)] and Bhaskar Kaviraj[1,a)]

AFFILIATIONS

[1] Department of Physics, School of Natural Sciences, Shiv Nadar University, Goutam Budha Nagar, Uttar Pradesh 201314, India
[2] Department of Physics, Indian Institute of Science Bangalore, Bangalore 560012, India
[3] School of Mechanical Engineering, Sungkyunkwan University, Suwon, South Korea

[a)] **Authors to whom correspondence should be addressed:** budhisingh025@gmail.com and bhaskar.kaviraj@snu.edu.in

ABSTRACT

MoS_2 based materials are considered the most reliable alternative catalysts for the hydrogen evolution reaction (HER), where engineering of active sites has emerged as an acceptable approach to tune their HER activity. In this approach, the dispersion of bulk MoS_2 in the aqueous phase was increased with a surfactant (sodium dodecyl sulfate), which reduced the exfoliation time and enhanced the exfoliation ability to produce layered MoS_2 nanosheets. During the hydrothermal treatment, the nanosheets were further scissored into small nanocrystals. Nanocrystals have attractive properties with stable dispersion and high-water solubility. Our method provides a scalable, eco-friendly, easy, and low-cost strategy for designing other HER catalysts. Such ultra-small MoS_2 nanocrystals with rich Mo vacancies were used as catalysts for HER, which showed excellent electrocatalytic activity with a low overpotential (95 mV) and small Tafel slope (41 mV/dec) in 0.5M H_2SO_4 electrolyte. The design and synthesis of the HER catalyst in this work presents a promising path for preparing active and stable electrocatalysts to replace costly metal-based catalysts for hydrogen production.

INTRODUCTION

Renewable energy sources are similar to flying stars and are the only alternative among all energy sources. Hydrogen has received much attention for renewable energy technologies because of its broad applicability and its ability to produce and supply energy with nearly zero carbon dioxide. Over recent decades, considerable effort has improved hydrogen production efficiency.[1–5] Nevertheless, the high cost and deficiency of noble metals have prevented large-scale hydrogen energy production. Therefore, fundamental requirements for designing and producing an alternative catalyst should be low cost, high activity, high stability, high availability, and a convenient synthesis procedure.[6–10]

Hydrogen, yielded by electrocatalytic water splitting can result in zero greenhouse gases. The advancement of platinum-free electrocatalysts (Pt) is a fundamental challenge in improving the overall efficiency of the hydrogen evolution reaction (HER), particularly in the case of resource insufficiency and an energy crisis. Theoretical research has demonstrated that the edges of MoS_2 nanostructures are the cause of efficient HER activity, which plays a vital role in manufacturing hybrid electrocatalysts. Therefore, the growth of MoS_2 based catalysts with rich active edge sites and available electrochemical surface area is vitally important for improving the overall efficiency of the HER. Tremendous effort has been made to enhance the HER activities of MoS_2 based catalysts by nanostructure engineering, defect engineering, phase engineering, and heteroatom doping to increase the number of intrinsic active sites.[11,12,50,52,54] Defect formation may change the crystal structure of MoS_2 and provide a different chemical and electronic environment.[13–15] The catalytic performance of defect-rich MoS_2 nanostructures has been studied in depth. These findings are of great importance for improving the material properties. Feng used first-principles calculations to study the structure and photoelectric properties of single-layer MoS_2 with Mo vacancies.[16–18] The effectiveness of Mo vacancies

strengthens the Mo–S bond. Several studies on the development of S vacancies in MoS_2 co-catalysts have been reported; however, there are few reports on creating Mo-vacancy rich MoS_2 co-catalysts to enhance the HER activity.[19–22]

Numerous approaches, including mechanical exfoliation, chemical exfoliation, lithium-ion intercalation, and chemical vapor deposition, have been developed to synthesize MoS_2 nanostructures. Although a comprehensive study has been carried out, many problems still need to be resolved before studying their unique characteristics for catalytic and electrochemical applications.[23] The top-down synthesis of high-quality TMDs (transition metal dichalcogenides) nanocrystals has been highly challenging because of their minute size, which requires time-consuming exfoliation and ultrasonication methods beginning from bulk TMD precursors (i) peeled to 2D TMD nanosheets first and (ii) further scissoring them down to nanocrystals.[24] Further defect engineering of the as-synthesized nanocrystals will provide exploration of more features of nanocrystals for catalytic and electrochemical applications.

In this approach, suitable molybdenum and sulfur precursors with adequate surfactants undergo hydrothermal treatment. The HER activity of the as-synthesized MoS_2 nanosheets and nanocrystal electrocatalysts was studied in acidic and alkaline media, and the HER activity of the synthesized MoS_2 nanosheets and nanocrystal electrocatalysts was studied in acidic and alkaline media. The as-synthesized MoS_2 nanocrystals showed a lower onset overpotential of 95 and 198 mV with a Tafel slope of 41 and 47 mV/dec for 0.5M H_2SO_4 and 1M KOH electrolytes, respectively, with a current density of 10 mA/cm^2. In addition, electrochemical impedance spectroscopy (EIS) was performed to assess the catalytic activity of the MoS_2 nanostructures and calculate their active electrochemical surface area (ECSA). The improved intrinsic activity of the catalyst indicates defect formation in MoS_2 nanocrystals. This was ascribed to the formation of more defects on the catalyst's surface. This was ascribed to many defects on the surface of the catalyst. The proposed approach has unique advantages over current procedures: (1) the synthesis time is considerably reduced and (2) the process is eco-friendly. Ultra-small MoS_2 nanocrystals exhibit better HER activity without metal heteroatoms or chemical reagents. In addition, MoS_2 nanostructures offer excellent performance and stability in acidic media, allowing them to be versatile catalysts for the HER. The noticeably improved active edges can increase the number of catalytic sites and stimulate the catalytic activity. It also facilitates charge-carrier transfer during the catalytic process for the evolution of H_2.

METHODS

Reagents and chemicals

Bulk molybdenum disulfide (MoS_2 powder, 99.9%, Product Number: 69860), dodecyl sodium sulfate [$CH_3(CH_2)_{11}OSO_3Na$, Product Number: 436143], sulfuric acid (H_2SO_4, Product Number: 339741), and potassium hydroxide (KOH, Product Number: 484016) were purchased from Sigma-Aldrich.

Experimental section

The MoS_2 nanocrystals were synthesized using single-bath sonication and hydrothermal treatment of commercial MoS_2 powder. In the first step, MoS_2 nanosheets were obtained through the liquid-phase exfoliation of MoS_2 powder. Usually, 1.4 g of MoS_2 powder and 0.5 g of SDS (sodium dodecyl sulfate) were mixed and dispersed in 120 ml of deionized water. After ultrasonication for 6 h, the solution mixture was centrifuged for 30 min at 8000 rpm to separate the unexfoliated MoS_2 sediment. During ultrasonication, the operating power was 120 W. We worked on a bath sonicator built by OSCAR ULTRASONIC (Model Number: Microclean 103).

The supernatant was carefully pipetted from the uppermost portion, and the dispersion was maintained for 2 h for sedimentation. The MoS_2 nanosheets were appropriately mixed in deionized water through sonication and centrifuged at 10 000 rpm two times to remove excess SDS. Finally, the as-synthesized MoS_2 nanosheets were dispersed in 50 ml of deionized water and placed in a 100 ml Teflon autoclave, which was then kept inside a muffle furnace at 180 °C. After heating for 5 h, it was naturally cooled to room temperature. The solution was then allowed for filtration through a 0.22-μm polytetrafluoroethylene (PTFE) filter, and the filtrate was washed by dialysis in water to remove impurities. Then, the as-synthesized nanocrystals were diluted with 10 ml of deionized water for further use (at 4 mg/ml).

Characterization: A UV-2401(Shimadzu Corporation) spectrophotometer was employed to investigate the absorption spectra of the MoS_2 nanostructures. The crystal structures of the bulk powder, nanosheets, and as-grown nanocrystals were examined using a Rigaku Miniflex diffractometer with a typical x-ray tube (Cu Kα radiation, 40 kV, 30 mA). Structural analysis of the MoS_2 nanostructures was performed using a transmission electron microscope (TEM) (Model JEOL JEM-2100F) at the voltage of 200 kV. TEM analysis was performed by drop-casting the dispersed MoS_2 nanostructures over a carbon-coated copper grid, followed by drying. The Raman spectra of the MoS_2 nanocrystals were obtained using a Renishaw Raman microscope using a 532 nm (0.3 mW) laser. Photoluminescence (PL) spectra were acquired with a Fluoromax 4C HORIBA Scientific spectrofluorometer upon excitation of a range of wavelengths using a 450 W xenon lamp. An XPS study was conducted on an ESCALAB 250Xi spectrometer (ThermoFisher) with an Al Kα x-ray source.

RESULTS AND DISCUSSION

As shown in Fig. 1, MoS_2 nanocrystals were sequentially synthesized through a combination of ultrasonication and a hydrothermal method from MoS_2 powder. In our approach, SDS was favored as a surfactant. The exfoliation time of nanosheets was reduced to 6 h, as was the case for the ultra-sonication exfoliation of MoS2 nanosheets in organic solvents, such as dimethylformamide (DMF) and *n*-methyl-2-pyrrolidone (NMP). It is understood that MoS_2 nanosheets tend to restack owing to the interlayer binding energy. Coleman *et al.* reported that few-layer TMDs could be synthesized by sonication in water if a surfactant stabilizer was added to prevent the re-aggregation induced by the significant surface energy.[25] Figure 2(a) consists of a couple of Mo 3d and S 2s core level peaks and is presented with two Mo 3d doublets and two singlet peaks (S 2s). The typical intense doublet peak, located at 230 eV, is assigned to Mo^{4+} (i-Mo^{4+}) and the charge state of molybdenum

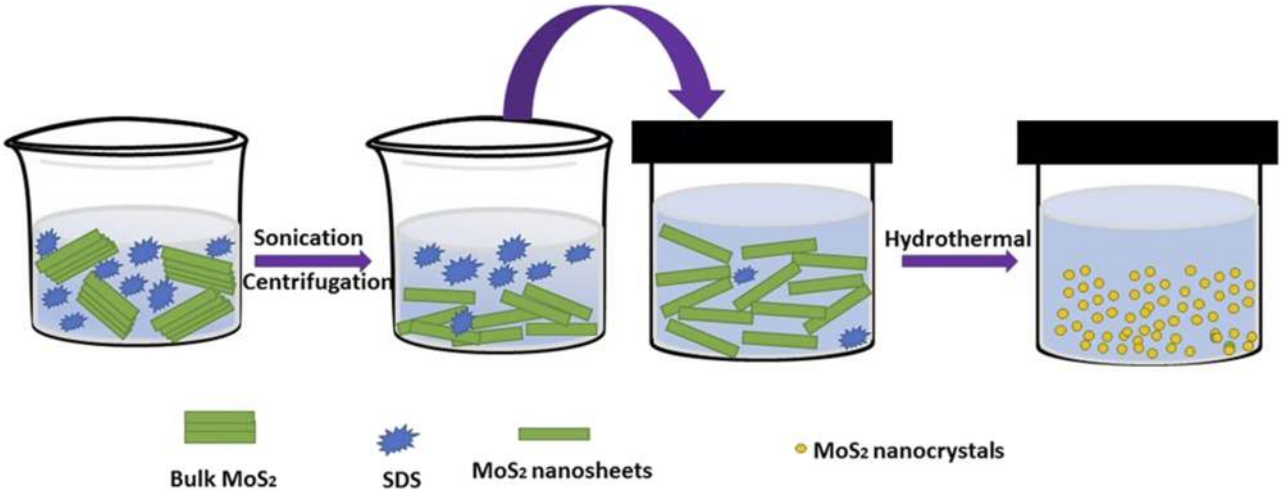

FIG. 1. Synthesis process of MoS_2 nanocrystals.

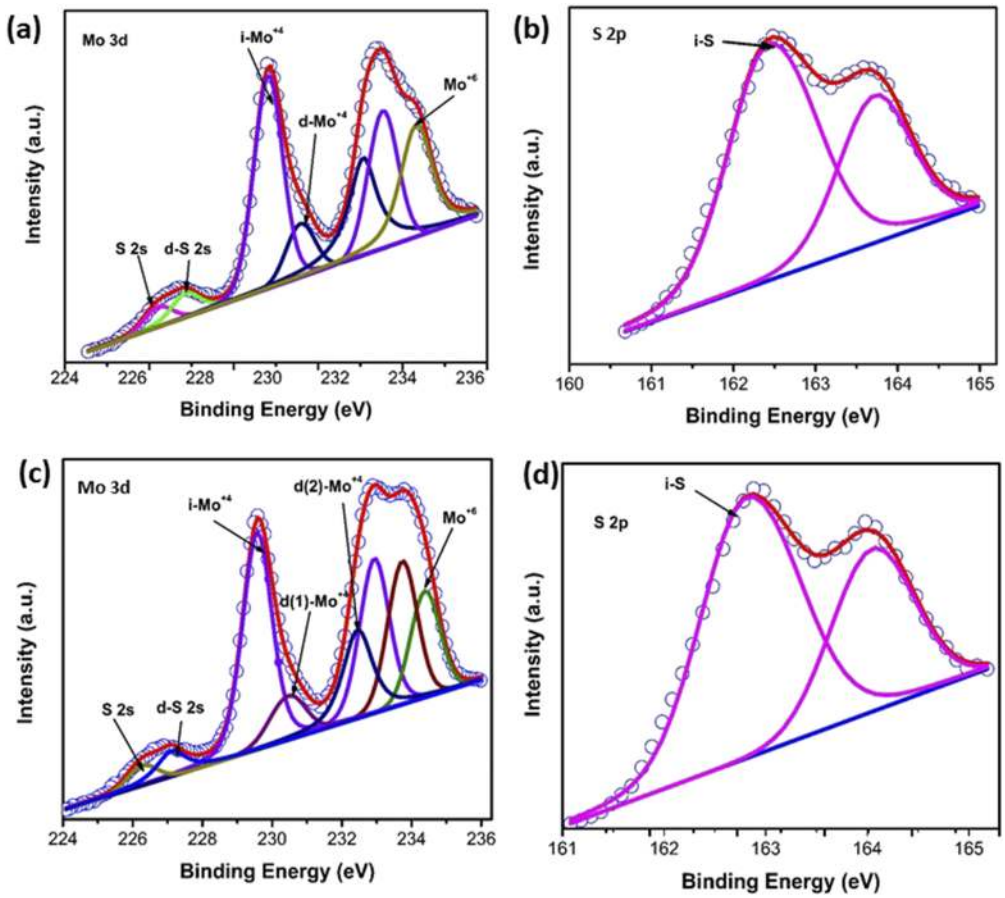

FIG. 2. High-resolution XPS survey spectra of the as-prepared bulk MoS_2. (a) Mo 3d and (b) S 2p spectra of MoS_2 nanosheets; (c) Mo 3d and (d) S 2p of nanocrystals.

in MoS_2. The doublet peak at 1.2 eV higher than binding energy (BE) originates from the defect Mo^{4+} (d-Mo^{4+}), assigned to Mo atoms neighboring sulfur vacancies (V_S). Ultimately, the peak at 234.4 eV is because of the Mo^{+6} species. They confirm that the Mo edges in MoS_2 nanocrystals are partly oxidized during the transition from the Mo^{4+} state to the Mo^{6+} state. The singlet peak is due to the S 2s emission from defect-free region of MoS_2, while the new singlet peak at 227.5 eV resembles sulfur near to a defect. The sulfur chemical environment can be analyzed precisely through the S 2p core level spectrum, exhibited in Fig. 2(b), where two doublets are found at 162.8 and 164.08 eV, respectively. We assign the most intense peak to intrinsic S (i-S) and the higher BE doublet to sulfur near S vacancies (d-S). In addition, the XPS measurement results also show that after hydrothermal treatment of the nanosheets, the stoichiometric ratio of Mo:S in the MoS_2 nanosheets and nanocrystals continuously changed from 1:2.443 to 1:2.602, showing that a large number of Mo vacancies (defects) are generated in MoS_2 after the hydrothermal treatment, which is dependent on the degree of disorder. Figure 2(c) shows the XPS spectrum of the Mo 3d core level region of the MoS_2 nanocrystals, which, apart from a slight chemical shift due to band bending, shows a different line shape than the nanosheets. This additional peak at 232.47 eV [d (2)-Mo^{4+}] corresponds to Mo atoms near a more complex defect that exists in the MoS_2 nanocrystal. Figure 2(d) shows S 2p spectra of MoS_2 nanocrystals. It is difficult to distinguish which defects are produced after hydrothermal treatment because a complex defect results in a higher BE than d (1)-Mo^{+4} and i-Mo^{+4}. It can be concluded that the Mo:S ratio decreased after hydrothermal synthesis, confirming the loss of Mo atoms.[26] The XPS survey scans confirmed the presence of Mo, S, O, and C elements [Figs. S4(e) and S4(f)]. A significant portion of carbon content [as shown in Figs. S2(a) and S2(c)] originated during the mounting of the samples to the XPS chamber. As exhibited in Figs. S2(b) and S2(d), the O 1s peak at 533 eV is attributed to the binding energy of oxygen in the Mo (IV)–O_2 bonds, thus confirming oxygen incorporation rather than surface oxidation. A fraction of oxygen could be incorporated into the carbon atoms existing on the surface of the samples and not to Mo. In addition, the XPS survey spectra of Mo 3d and S 2p are shown in Figs. S3(a) and S3(b).[27–29]

The crystal structures of the as-prepared MoS_2 samples, including bulk precursors, were characterized by x-ray diffraction (XRD) [Fig. 3(a)]. Bulk MoS_2 shows a high-intensity peak at $2\theta = 14.5^\circ$, corresponding to the (002) plane, accompanied by other characterized peaks indicating a substantial number of grains in this precise orientation. The MoS_2 nanosheets have three prominent peaks at 2θ values of 14.5°, 33.25°, and 57.56°, corresponding to the (002), (013), and (012) orientations. After hydrothermal treatment, the (002) peak of the as-synthesized MoS_2 nanocrystals nearly disappeared, confirming the formation of few-layer nanocrystals, as supported by the TEM results. Moreover, the minute peak at $2\theta = 22.4^\circ$ appeared from the partial restacking of the nanocrystals during the coating process. The XRD spectra of the nanosheets, nanocrystals, and bulk MoS_2 are perfectly matched with the 2H–MoS_2 crystal symmetry.[30] Figure 3(b) shows the Raman characteristics of the MoS_2 nanosheets, nanocrystals, and bulk samples. Bulk MoS_2 shows two distinct peaks, E^1_{2g} and A_{1g}, with a frequency difference of 25 cm^{-1} due to the stacking of neighboring S–Mo–S layers. The E^1_{2g} and A_{1g} peaks correspond to in-plane phonon and out-of-plane vibration modes, respectively, indicating the existence of the 2H-phase alone. The observed peak difference (24.07 cm^{-1}) for the MoS_2 nanocrystals is less than the bulk precursor, indicating that these MoS_2 nanocrystals contain a few-layered composition.[31]

The absorption spectra of the nanocrystals, nanosheets, and bulk MoS_2 are shown in Fig. 4(a). The excitonic peaks positioned at A and B show a direct band-to-band transition at the K-point of the Brillouin zone. The peaks at C and D are due to the direct excitonic transitions from the split valence to the conduction band at the M point of the Brillouin zone. The energy splitting within different absorbance peaks in bulk MoS_2 arises from spin–orbit and interlayer coupling.[32] However, the interlayer coupling starts to diminish with a reduction in the number of layers. The absorbance peak at 350 nm in the MoS_2 nanocrystals is associated with the excitonic features. This validates the nanocrystals' size reduction

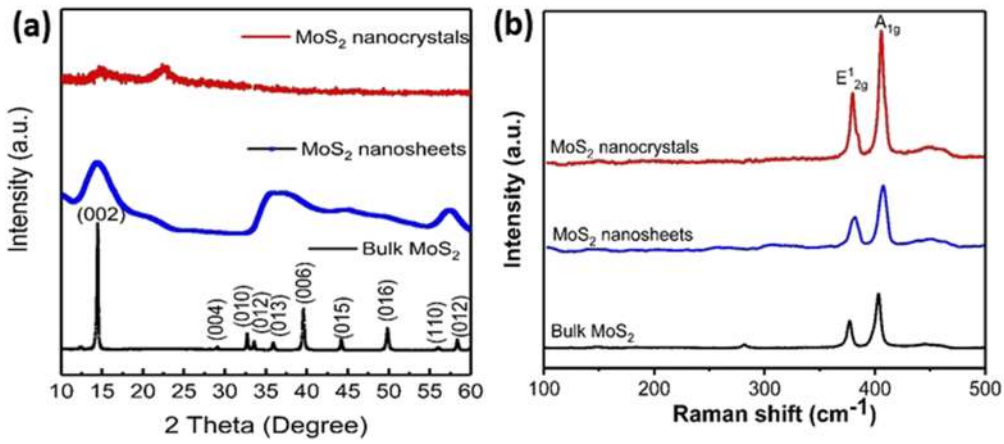

FIG. 3. (a) The x-ray diffraction pattern and (b) Raman spectra of bulk MoS_2, nanosheets, and nanocrystals.

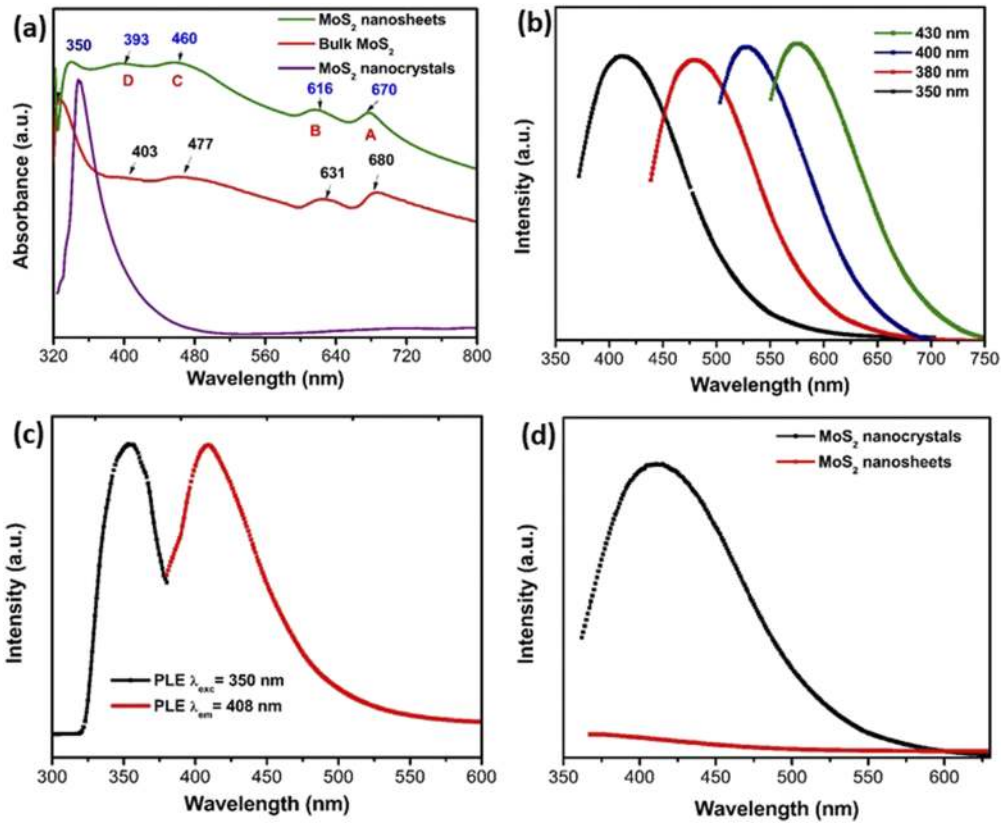

FIG. 4. (a) UV-VIS spectra of bulk MoS_2, nanosheets, and nanocrystals, (b) PL spectra of the monolayer MoS_2 nanocrystals at different excitation wavelengths, (c) PLE spectrum with the detection wavelength of 408 nm and PL spectrum excited at 350 nm of the MoS_2 nanosheets and MoS_2 nanocrystals, which were measured in water under the excitation of 350 nm, and (d) PL spectra of monolayer MoS_2 nanocrystals.

after the nanosheets' hydrothermal treatment. The shifting of the absorbance peak position toward shorter wavelengths with a particle size reduction is associated with the quantum size effect in the MoS_2 nanostructures.[33,34] PL and PL excitation (PLE) spectra [Fig. 4(c)], a prominent emission maximum at 408 nm, were observed when the nanocrystal sample was excited at 350 nm with a Stokes shift of 58 nm. PLE spectra [Fig. 4(c)] listed with a designed wavelength of 408 nm exhibited one peak at 350 nm. The photoluminescence spectra of the MoS_2 nanocrystal dispersion excited by varying wavelengths ranging from 350 to 430 nm are shown in Fig. 4(b). A redshift in the photoluminescence emission between 408 and 575 nm increased with the excitation wavelength. The emission from the quantum-sized MoS_2 nanocrystals may also appear from the surface state recombination.[35,36] Numerous atoms are at or near the edge of the nanocrystals, driving the dominance of dangling bonds and defects in the surface states. Foreign atoms added during the synthesis procedure can also produce further surface states, serving as traps or recombination sites. In a few nanometers of MoS_2 nanocrystals, the PL peak obtained at 408 nm is correlated with surface recombination. Furthermore, the emission centered at 408 nm was missing in the PL spectra of the as-prepared MoS_2 nanosheets, as shown in Fig. 4(d). This result can be related to the few edge defects and the larger MoS_2 nanosheets' dangling bonds. The chemical and optical properties of the MoS_2 nanocrystals were characterized from the different samples by Raman and UV–vis absorption spectroscopy [as shown in Figs. S1(a) and S1(b)]. The analysis results show that ultra-small MoS_2 nanocrystals can be successfully prepared. Figure S1(c) shows the brown-colored dispersed MoS_2 nanocrystals.[37,38]

The distinctive morphological and structural features of the as-synthesized MoS_2 nanostructures were examined using TEM. Figures 5(a) and 5(b) show low-magnification TEM and high-resolution TEM images of the MoS_2 nanosheet with selected area electron diffraction (SAED) pattern (the top right inset of the figure). Figure 5(a) shows the in-plane hexagonal arrangements, which show the crystalline features of the MoS_2 nanosheets, which are attributed to the (010), (011), and (002) planes of 2H–MoS_2, respectively [JCPDF-00-037-1492]. The lattice fringe of MoS_2 nanosheets with an interplanar spacing of 0.612 nm corresponds to the (002) lattice plane of MoS_2 [as shown in the bottom left inset of Fig. 5(b)]. The MoS_2 nanocrystal size ranges from 2 to 5 nm with an average size of 3 ± 0.2 nm with no particle aggregation, as shown in the inset of Fig. 5(c). The HRTEM image of the nanocrystals [top left inset of Fig. 5(d)] reveals disordered lattice fringes.

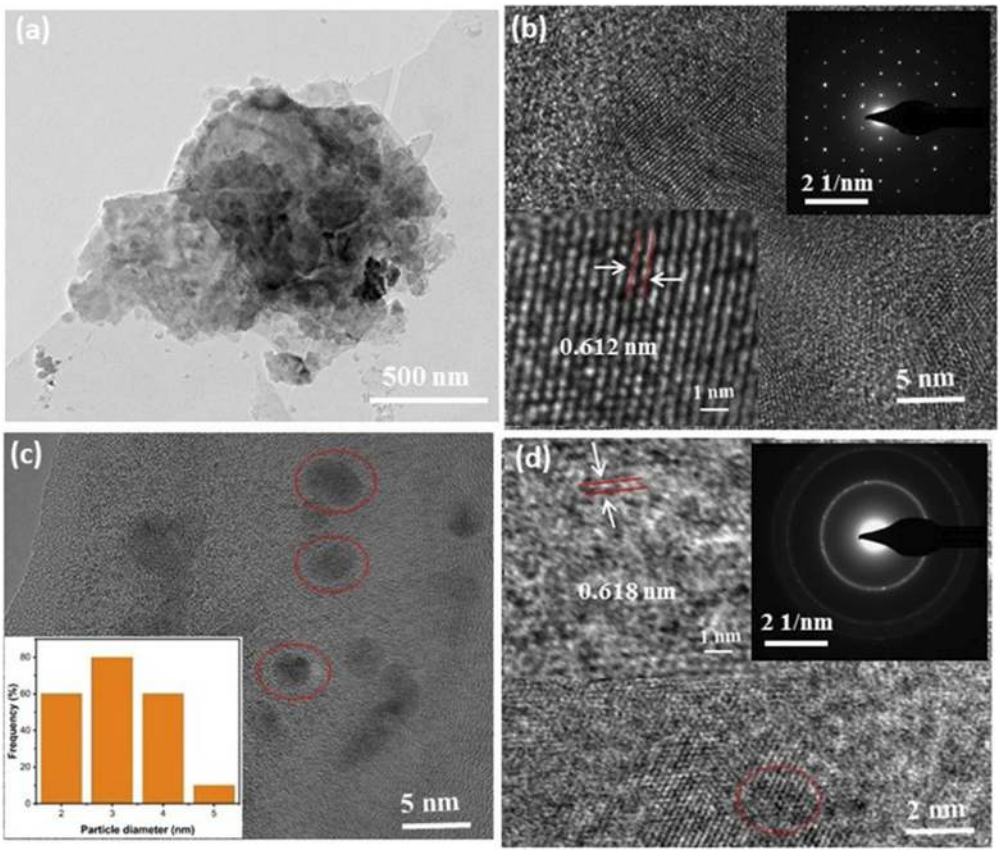

FIG. 5. (a) Low-magnification TEM image of MoS_2 nanosheets. (b) HRTEM image of MoS_2 nanosheets [the top right corner inset shows the corresponding selected electron diffraction (SAED) pattern of the as-synthesized nanosheets, and the bottom left corner inset shows the corresponding lattice fringes]. (c) HRTEM image of MoS_2 nanocrystals (the inset shows the histogram of size distribution). (d) Zoomed HRTEM image [the top right corner inset shows the corresponding selected electron diffraction (SAED) pattern of the as-synthesized nanocrystals, and the top left corner inset shows the corresponding lattice fringes].

It is worth noting that the lattice fringes are discontinuous and can be associated with rich defects. These defects act as significant parameters that determine the high performance of the catalyst for the HER. The corresponding SAED pattern shows a diffuse ring pattern related to the polycrystallinity of the MoS_2 nanocrystals, attributed to the (002) plane of MoS_2 [inset of Fig. 5(d)]. The lattice spacing (d) was 0.618 nm, which corresponds to the (002) plane of MoS_2.[39–42]

The HER activity of different electrocatalysts was studied in 1M KOH and 0.5M H_2SO_4 electrolyte solutions using a three-electrode system (Auto lab/PGSTAT128N) with a standard glassy carbon (GC) working electrode (GCE, 1 mm diameter). For linear swipe voltammetry studies, the GCE was modified using a MoS_2 catalyst (40 μl of nanosheets, nanocrystals, and bulk MoS_2). The MoS_2 suspension in water was drop-cast onto glassy carbon as the working electrode and dried overnight in an inert environment. The mass loading of the catalyst deposited on the electrode was 116 $\mu g/cm^2$, which was the same for each measurement. The working electrode potential in the LSV (linear swipe voltammetry) measurement ranged from 0 to −0.4 V with Ag/AgCl at a scan rate of 2 mV/s in 0.5M H_2SO_4 and −0.15 to −0.55 V in 1M KOH. A graphite rod and Ag/AgCl electrode were employed as the counter and reference electrodes.

In contrast, the bare GCE and bulk MoS_2 showed relatively poor HER catalytic activity with the current density value of 10 mA/cm^2 and a large onset overpotential. For bulk MoS_2, the onset overpotential was 142 mV in H_2SO_4 and 385 mV in KOH with a weak cathodic current density. As the cathodic current density is proportional to the evolved hydrogen, the large current density confirms an excellent hydrogen evolution reaction. The outstanding catalytic performance of MoS_2 nanocrystals can result from the abundance of active sites and the presence of defects in the sample.[43–48]

A schematic of the HER activity of the as-synthesized MoS_2 samples is shown in Figs. 6(a) and 7(a) for different electrolytes. Furthermore, it was observed that the combination of bath sonication and hydrothermal treatment enhanced the catalytic activity of MoS_2 nanocrystals for HER [as shown in Figs. 6(b) and 7(b)]. The as-synthesized MoS_2 nanocrystals showed much higher HER activity with a low onset overpotential of 95 and 198 mV in H_2SO_4

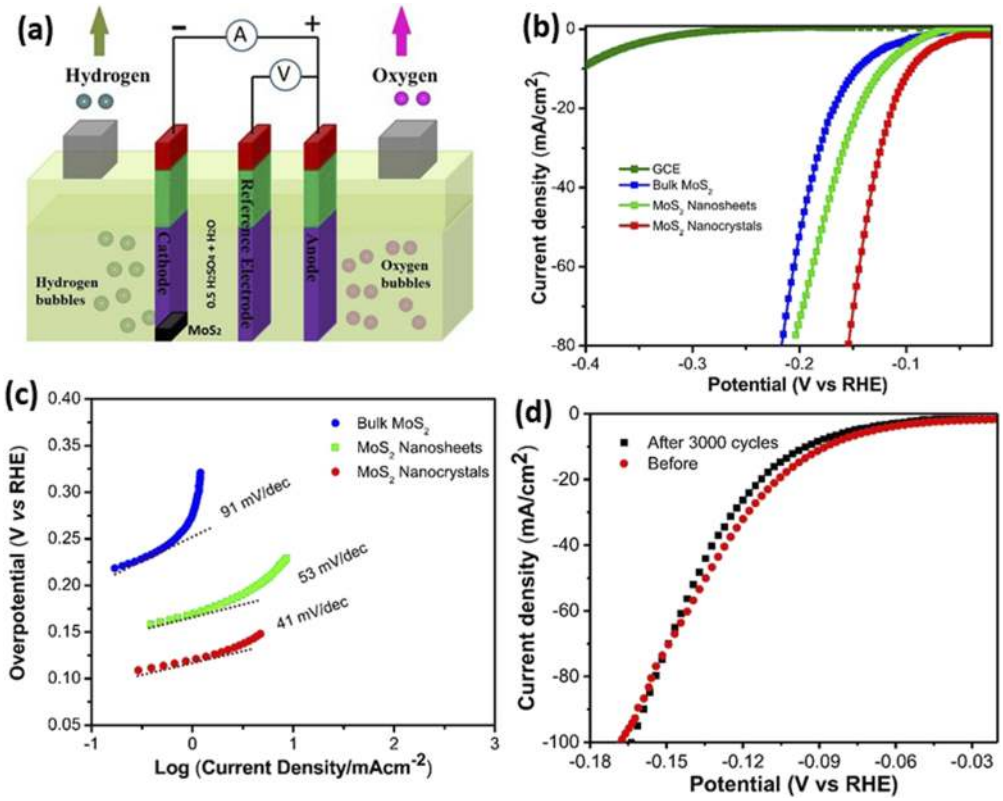

FIG. 6. (a) Schematic of the HER activity in 0.5 M H_2SO_4. (b) LSV curves of all samples in 0.5 M H_2SO_4. (c) Tafel plots of GCE, bulk MoS_2, nanosheets, and nanocrystals. (d) Stability test of MoS_2 nanocrystals.

and KOH at a current density of 10 mA/cm^2.[50–54] Tafel analysis is a robust tool for determining the HER catalytic activity of catalysts. This reveals the inherent properties of the materials, followed by the rate-determining steps involved in electrocatalysis.[49]

Furthermore, the surface kinetics of electrocatalytic materials can be studied using the Tafel slope. An electrocatalytic element with a small Tafel slope value is regarded as a more desirable electrocatalyst because it enhances hydrogen production at a greater rate and raised potential. The Tafel plot represents the relationship of steady-state current densities at various overpotentials to increase the reaction rate by a factor of ten, calculated by the extent of the variation in the activation energy for a presented increment overpotential. The Tafel slope was obtained by fitting the linear portion of the Tafel plot to the Tafel equation: $\eta = b\log(j) + a$, where η denotes the overpotential, j denotes the current density, a constant, and b is the Tafel slope.[51,53] Figures 6(c) and 7(c) exhibit the Tafel plots of the as-synthesized MoS_2 nanocrystals, nanosheets, and bulk MoS_2. The Tafel slopes of the MoS_2 nanocrystals in 0.5M H_2SO_4 and 1M KOH are 41 and 47 mV/dec, respectively. A comparison of the HER activities of the MoS_2-based catalysts is shown in Table I. The Tafel slopes for MoS_2 nanosheets are ~53 and ~64 mV/dec, whereas bulk MoS_2 shows Tafel slopes of ~91 and 96 mV/dec for 0.5M H_2SO_4 and 1M KOH electrolytes, respectively. The working electrode potentials were referenced to a reversible hydrogen electrode using Eq. (1),[49]

$$E_{RHE} = E_{Ag/AgCl} + 0.0591PH + 0.1976. \quad (1)$$

In this study, the Tafel slope of 41 mV/dec for MoS_2 nanocrystals implies that HER was most probably controlled by electron reduction of protons, which gives a hydrogen atom associated to an active site (Volmer reaction) and electrochemical desorption of hydrogen (Heyrovsky reaction). The small Tafel slope of the defect-rich MoS_2 nanocrystal is helpful for possible purposes because it will drive a faster increase in the HER activity (hydrogen production) with increasing overpotential. First, a tiny grain size of nanocrystals could provide the maximum reaction sites for the HER. Second, the hydrothermal treatment produces more Mo-vacancies in MoS_2, which increases the HER activity of MoS_2 due to increased reaction sites.[55] This high current density value can be assigned to the unique defect-rich structure and morphology that provide more reactive sites.[63–65] For bulk MoS_2 (116 mV/dec), the ineffective edges restrict kinetic response, where adsorption occurs, as shown by the large Tafel slope. Various studies have proposed the HER mechanisms in the acid and found that HER involves three steps in an acidic medium: (i) $H_3O^+ + e^- \rightarrow H_{ads} + H_2O$ (initial discharge or Volmer step), (ii) $H_3O^+ + H_{ads} + e^- \rightarrow H_2 + H_2O$ (atom + ion or Heyrovsky step), and (iii) $H_{ads} + H_{ads} \rightarrow H_2$ (atom + atom or Tafel step), which is different from the mechanism in an alkaline medium. Likewise, the HER mechanism in the alkaline medium can also carry

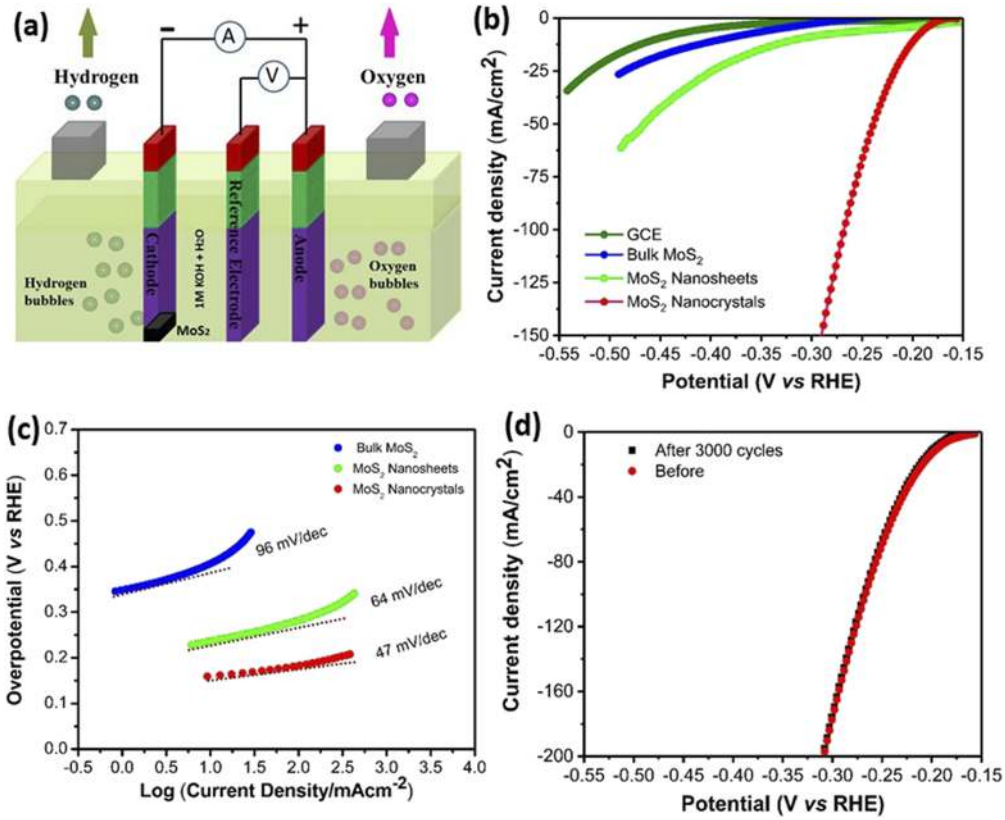

FIG. 7. (a) Schematic of the HER activity in 1M KOH. (b) LSV curves of all samples in 1M KOH. (c) Tafel plots of Pt, GCE, bulk MoS_2, nanosheets, and nanocrystals. (d) Stability test of MoS_2 nanocrystals.

the Volmer–Heyrovsky step or Volmer–Tafel step, as shown in the above equations.

In contrast to the acidic conditions where water is electrochemically dissociated into adsorbed OH^- and H^* in the Volmer step, in an alkaline medium, the catalyst needs to break the stronger covalent H–O–H bond before adsorbing H^*, rather than the covalent bond of the hydronium ion so that the reduction of H_3O^+ could quickly proceed.[63–66] Usually, though, it has been noticed that HER activities are driven faster in acid than alkaline electrolytes. With inherent interest, the urge to explore and ultimately discover the difficult contribution of pH comes from the stability effects that disturb most non-precious metallic catalysts in acid solutions. Therefore, switching to an alkaline environment is necessary for designing platinum-free HER catalysts. Despite the pH parameter, the nature

TABLE I. Comparison of electrochemical performance of MoS_2 nanocrystals toward HER activity with other catalys.

Catalyst	Electrolyte	Overpotential (mV)	Tafel slope (mV/dec)	References
MoS_2 nanosheets/strained S vacancies	0.5 M H_2SO_4	170	60	70
P-doped 2H–MoS_2 nanosheets	0.5 M H_2SO_4	300	49	71
MoS_2/reduced graphene oxide	0.5 M H_2SO_4	140	41	72
Ni-doped MoS_2 nanosheets	1 M KOH	98	60	73
MoS_2@Ni/carbon cloth	1 M KOH	91	89	74
Ni-doped MoS_2/Ni foam	1 M NaOH	207	65	71
MoS_2 nanocrystals	1 M KOH	198	47	This work
	0.5 M H_2SO_4	**95**	**41**	

of the proton source and surface morphology play a crucial role in determining hydrogen electrocatalysis from an experimental point of view. However, to fabricate novel materials for HER, we have to distinguish the governing phenomena under all pH conditions and then search for various combinations of different atoms working as the active sites, which can also be enhanced by using distinct morphologies as found in engineered nanostructures.[56–58,70–74]

In addition to the HER activity, stability is another outstanding quality of an advanced electrocatalyst. A stability test was conducted using MoS_2 nanocrystals in the HER. The stability of the as-synthesized MoS_2 nanocrystals was measured by taking 3000 continuous CV cycles within the voltage window of −0.3 and 0.01 V and −0.55 and −0.15 in 0.5M H_2SO_4 and 1M KOH electrolytes, respectively, vs reversible hydrogen electrode (RHE) with the scan rate of 100 mV/s to reach 10 mA/cm^2 without iR correction. Figures 6(d) and 7(d) show that after 3000 cycles, the catalyst maintains high HER activity with negligible degradation in 0.5 M H_2SO_4 and 1 M KOH.

The impedance behavior of the MoS_2 nanocrystals and nanosheets was investigated in the linear potential region of the Tafel plots [Figs. 8(a) and 8(b)] between 80 and 110 mV of overpotential in 0.5 M H_2SO_4. The large semicircles at the low-frequency end are potentially dependent, describing a charge transfer process; the quicker the charge transfer, the higher the inverse of the charge transfer resistance ($1/R_{ct}$).[59] On the other hand, the high-frequency semicircles are potentially self-governing [the Ohmic series resistance (R_S)] and describe the connection between the GCE and the electrocatalyst. The solid-state interface layer's chemical capacitance (CPE) was built during the passivation reaction. A fitted electrical circuit [exhibited in the inset of Fig. 8(c)] was used to study the impedance behavior of the MoS_2 catalysts, and a perfect fit can be observed at various overpotentials. The R_{ct} data extracted from

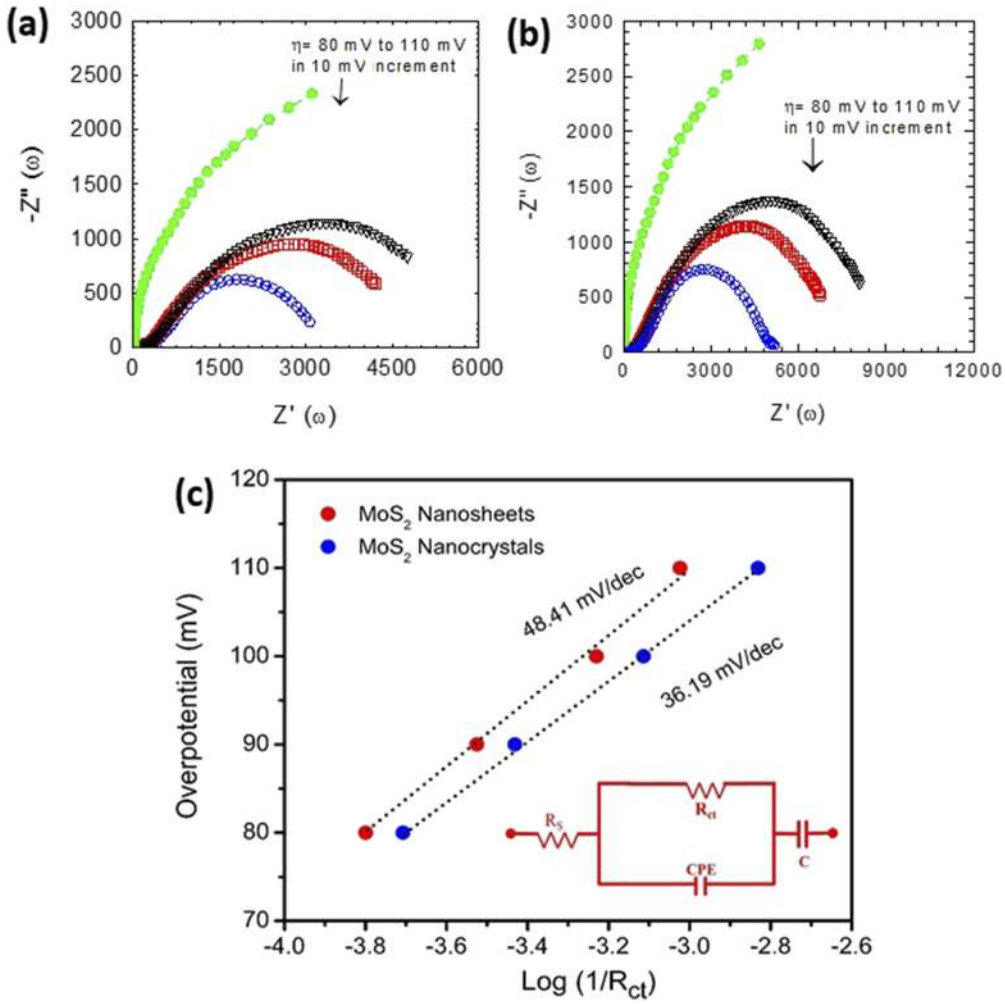

FIG. 8. Nyquist plots of (a) MoS_2 nanocrystals and (b) nanosheets as a function of overpotential ranging from 80 to 110 mV with an increment of 10 mV. (c) Corresponding Tafel plots of catalysts, which were obtained using R_{ct} data from the impedance analysis.

Figs. 8(a) and 8(b) were used to obtain Tafel plots for the MoS_2 nanocrystals and nanosheets, respectively. Figure 8(c) shows a linear relationship between the overpotential and $\log(1/R_{ct})$, with Tafel slopes of 36.19 and 48.41 mV/dec, respectively, for MoS_2 nanocrystals and nanosheets, which shows that the HER rate is usually higher when the nanosheets are engineered to defect-rich nanocrystals. The Tafel slopes obtained using the voltammetric and EIS methods were not comparable for both catalysts. This variation can be attributed to the electronic transport resistance inherent in MoS_2 incorporated in the voltammetry data, removed in the EIS analysis. Thus, the EIS method of Tafel analysis revealed pure charge transfer kinetics of the HER. The actual HER kinetics were suppressed in the voltammetric method of Tafel analysis because of the resistance resulting from the several components of R_s and the resistance due to slow electron transport. Hence, EIS was used in a comprehensive Tafel analysis to avoid the above constraint. Tafel's analysis showed the process of the Volmer–Heyrovsky mechanism with a rate-determining Heyrovsky step in MoS_2 electrocatalysts.[60–62]

Furthermore, the active sites of the catalysts are another parameter to illustrate this phenomenon.[68–70] The effective electrochemical active surface area (ECSA) of MoS_2 nanocrystals and nanosheets with comparable composition is proportional to the electrochemical double-layer capacitance (C_{dl}), which was evaluated by CV in a non-Faradaic region at different scan rates (V_b) of 20, 40, 60, 80, and 100 mV/s [Figs. 9(a) and 9(b)]. Then, the double-layer capacitance (C_{dl}) was calculated by plotting $d(\Delta j) = (j_a - j_c)$ as a function of the scan rate [Figs. 9(c) and 9(d)]. It can be calculated using Eq. (2),[67]

$$C_{dl} = \frac{d(\Delta j)}{2dV_b}.$$

The ECSA can be calculated from C_{dl} according to Eq. (3),

$$ECSA = \frac{C_{dl}}{C_s},$$

where C_s indicates the value of specific capacitance of the MoS_2 catalyst or the atomically smooth planar surface of the substance per unit area under identical electrolyte conditions; the estimated value of ECSA for MoS_2 nanocrystals is ~34 cm^2. In comparison, the value of ECSA for the MoS_2 nanosheet samples was ~28 cm^2. Overall, the superior long-term stability, higher electrochemical surface area, lower Tafel slope, and low overpotential in defect-engineered MoS_2 give an efficient hydrogen evolution reaction.

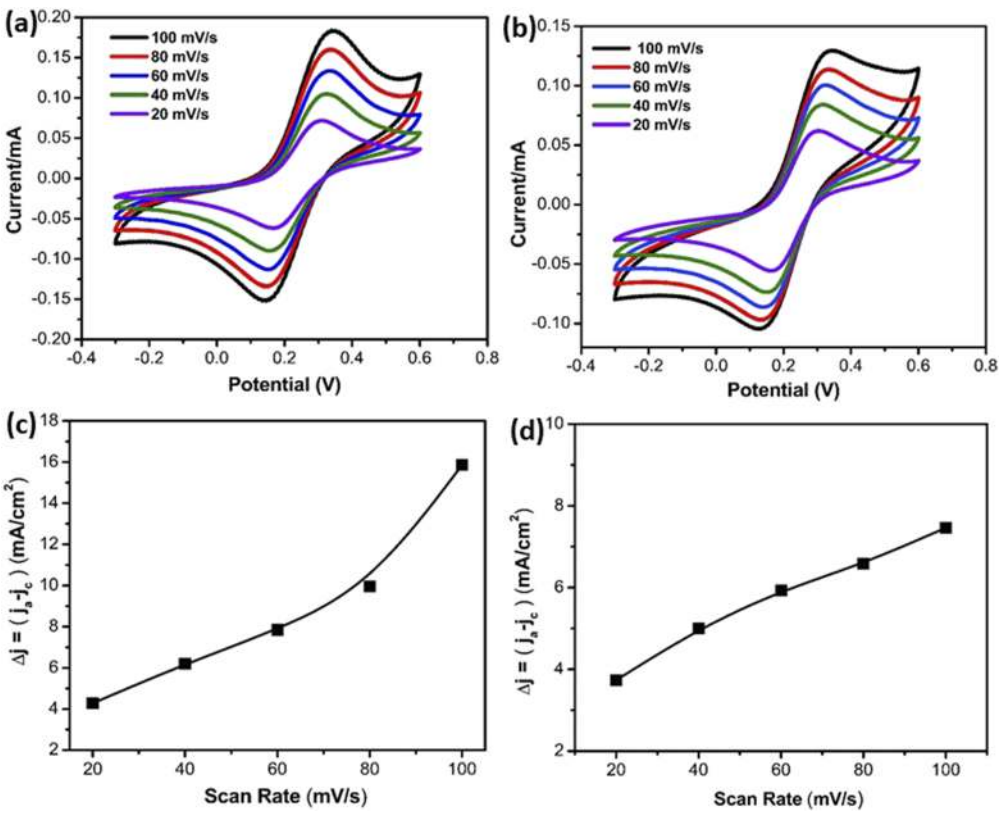

FIG. 9. Cyclic voltammetry curves of (a) MoS_2 nanocrystals and (b) MoS_2 nanosheets at scan rates (V_b) from 20 to 100 mV/s. Scan rate dependence of the current densities of (c) MoS_2 nanocrystals and (d) MoS_2 nanosheets.

CONCLUSIONS

This study used a facile route to synthesize defect-rich MoS_2 nanocrystals in an aqueous solution through ultrasonication and hydrothermal treatment. It is an environmentally friendly process, as organic solvents are not used throughout the synthesis. The ability to exfoliate MoS_2 nanosheets considerably increased with the SDS surfactant. The defect-engineered MoS_2 nanocrystals showed excellent HER activity compared to bulk and MoS_2 nanosheets in a 0.5 M H_2SO_4 electrolyte. The as-synthesized MoS_2 nanocrystal catalysts exhibited outstanding HER activity in an acidic medium with a low overpotential of ~95 mV and a Tafel slope of 41 mV/decade, thus demonstrating the Volmer–Heyrovsky mechanism for the HER activity. The morphology of MoS_2 nanocrystals and the increase in active sites result in excellent catalytic activity, supported by ECSA and EIS results. This process can be advanced to other systems to develop cost-effective catalysts with enhanced performance for large-scale applications.

SUPPLEMENTARY MATERIAL

See the supplementary material for Raman and UV–vis spectra of MoS_2 nanocrystals from different levels of vial containing dispersed MoS_2 nanocrystals, HRXPS spectra of C 1s, O 1s, and survey spectra of MoS_2 nanocrystals and nanosheets, XPS spectra of Mo 3d and S 2p of bulk MoS_2, and electrical parameters of the equivalent circuit obtained by fitting the EIS data.

ACKNOWLEDGMENTS

We acknowledge the support of Dr. Nasir Ali at the SKKU Advanced Institute of Nanotechnology (SAINT), Sungkyunkwan University 2066, Seobu-ro, Jangan-GU, Suwon, Gyeonggi-do 16419, Korea, for analysis of XPS findings. The authors would like to thank Dr. Jaivardhan Sinha in the Department of Physics and Nanotechnology, SRM Institute of Science and Technology, Kattankulathur, Kancheepuram, 603203, India, for the characterization of Raman and Dr. Rakesh Sharma from Shiv Nadar University for his help in characterization of the PL. We also appreciate Professor Subhasis Ghosh at Jawaharlal Nehru University, New Delhi, India, for scientific discussion.

The funders had no role in study design, data collection, analysis, decision to publish, or manuscript preparation.

AUTHOR DECLARATIONS

Conflict of Interest

The authors have no conflicts to disclose.

Ethics Approval

The Ethics Committee of Shiv Nadar University approved the study.

Author Contributions

D.S. conceptualized and planned the details of the experimental plans. D.S., J.S., and S.C. managed all experiments and necessary characterization. D.S. and B.K. appropriately did the scientific analysis and result confirmation, and D.S. drafted the article with the assistance of B.S. and B.K.

DATA AVAILABILITY

The data that support the findings of this study are available within the article and its supplementary material.

REFERENCES

[1] D. C. Binwal, K. Pramoda, A. Zak, M. Kaur, P. Chithaiah, and C. N. R. Rao, ACS Appl. Energy Mater. **4**, 2339 (2021).
[2] W. Zhou, L. Dong, L. Tan, and Q. Tang, J. Phys.: Condens. Matter **33**, 395002 (2021).
[3] H. Wang, H. Tang, and Y. Li, J. Phys. Chem. C **125**, 3337 (2021).
[4] D. Liu, Z. Lv, J. Dang, W. Ma, K. Jian, M. Wang, D. Huang, and W. Tian, Inorg. Chem. **60**, 9932 (2021).
[5] T. Zhang and A. B. Anderson, Electrochim. Acta **53**, 982 (2007).
[6] M. D. Sharma, C. Mahala, B. Modak, S. Pande, and M. Basu, Langmuir **37**, 4847 (2021).
[7] D. Sahoo, J. Shakya, N. Ali, W. J. Yoo, and B. Kaviraj, Langmuir **38**, 1578 (2022).
[8] A. Winchester, S. Ghosh, S. Feng, A. L. Elias, T. Mallouk, M. Terrones, and S. Talapatra, ACS Appl. Mater. Interfaces **6**, 2125 (2014).
[9] K. Chang *et al.*, Adv. Energy Mater **6**, 1502555 (2016).
[10] H. Ma, Z. Shen, and S. Ben, J. Colloid Interface Sci. **517**, 204 (2018).
[11] B. Hinnemann, P. G. Moses, J. Bonde, K. P. Jørgensen, J. H. Nielsen, S. Horch, I. Chorkendorff, and J. K. Nørskov, J. Am. Chem. Soc. **127**, 5308 (2005).
[12] T. F. Jaramillo, K. P. Jørgensen, J. Bonde, J. H. Nielsen, S. Horch, and I. Chorkendorff, Science **317**, 100 (2007).
[13] X. Li, Z. Wang, J. Zhang, C. Xie, B. Li, R. Wang, J. Li, and C. Niu, Carbon **85**, 168 (2015).
[14] H. Coy Diaz, J. Avila, C. Chen, R. Addou, M. C. Asensio, and M. Batzill, Nano Lett. **15**, 1135 (2015).
[15] Y. Ouyang, C. Ling, Q. Chen, Z. Wang, L. Shi, and J. Wang, Chem. Mater. **28**, 4390 (2016).
[16] L.-p. Feng, J. Su, and Z.-t. Liu, RSC Adv. **5**, 20538 (2015).
[17] H. F. Bettinger, J. Phys. Chem. B **109**, 6922 (2005).
[18] F.-J. Zhang, X. Li, X.-Y. Sun, C. Kong, W.-J. Xie, Z. Li, and J. Liu, Appl. Surf. Sci. **487**, 734 (2019).
[19] M. Ghorbani-Asl, S. Kretschmer, D. E. Spearot, and A. V. Krasheninnikov, 2D Mater. **4**, 025078 (2017).
[20] L.-p. Feng, H.-q. Sun, A. Li, J. Su, Y. Zhang, and Z.-t. Liu, Mater. Chem. Phys. **209**, 146 (2018).
[21] Z. Chen, D. Cummins, B. N. Reinecke, E. Clark, M. K. Sunkara, and T. F. Jaramillo, Nano Lett. **11**, 4168 (2011).
[22] X. Wang, Y. Zhang, H. Si, Q. Zhang, J. Wu, L. Gao, X. Wei, Y. Sun, Q. Liao, Z. Zhang, K. Ammarah, L. Gu, Z. Kang, and Y. Zhang, J. Am. Chem. Soc. **142**, 4298 (2020).
[23] D. Sahoo, S. P. Behera, J. Shakya, and B. Kaviraj, PLoS One **17**, e0260955 (2022).
[24] Y. Yan, C. Zhang, W. Gu, C. Ding, X. Li, and Y. Xian, J. Phys. Chem. C **120**, 12170 (2016).
[25] J. N. Coleman *et al.*, Science **331**(80), 568 (2011).
[26] A. Syari'Ati, S. Kumar, A. Zahid, A. Ali El Yumin, J. Ye, and P. Rudolf, Chem. Commun. **55**, 10384 (2019).
[27] W.-J. Xie, X. Li, and F.-J. Zhang, Chem. Phys. Lett. **746**, 137276 (2020).
[28] Z. He, R. Zhao, X. Chen, H. Chen, Y. Zhu, H. Su, S. Huang, J. Xue, J. Dai, S. Cheng, M. Liu, X. Wang, and Y. Chen, ACS Appl. Mater. Interfaces **10**, 42524 (2018).
[29] J. Xie, J. Zhang, S. Li, F. Grote, X. Zhang, H. Zhang, R. Wang, Y. Lei, B. Pan, and Y. Xie, J. Am. Chem. Soc. **135**, 17881 (2013).

[30]D. Sahoo, B. Kumar, J. Sinha, S. Ghosh, S. S. Roy, and B. Kaviraj, Sci. Rep. **10**, 10759 (2020).
[31]B. Li, L. Jiang, X. Li, P. Ran, P. Zuo, A. Wang, L. Qu, Y. Zhao, Z. Cheng, and Y. Lu, Sci. Rep. **7**, 11182 (2017).
[32]S. Xu, D. Li, and P. Wu, Adv. Funct. Mater. **25**, 1127 (2015).
[33]J. Kaur *et al.*, Sci. Rep. **8**, 16386 (2018).
[34]Y. T. Wang, C. W. Luo, A. Yabushita, K. H. Wu, T. Kobayashi, C. H. Chen, and L. J. Li, Sci. Rep. **5**, 8289 (2015).
[35]A. Splendiani, L. Sun, Y. Zhang, T. Li, J. Kim, C.-Y. Chim, G. Galli, and F. Wang, Nano Lett. **10**, 1271 (2010).
[36]D. B. Shinde and V. K. Pillai, Chem. - Eur. J. **18**, 12522 (2012).
[37]L. Bao, Z.-L. Zhang, Z.-Q. Tian, L. Zhang, C. Liu, Y. Lin, B. Qi, and D.-W. Pang, Adv. Mater. **23**, 5801 (2011).
[38]M. Zhang, L. Bai, W. Shang, W. Xie, H. Ma, Y. Fu, D. Fang, H. Sun, L. Fan, M. Han, C. Liu, and S. Yang, J. Mater. Chem. **22**, 7461 (2012).
[39]X. Ren, L. Pang, Y. Zhang, X. Ren, H. Fan, and S. Liu, J. Mater. Chem. A **3**, 10693 (2015).
[40]Z. Yin, H. Li, H. Li, L. Jiang, Y. Shi, Y. Sun, G. Lu, Q. Zhang, X. Chen, and H. Zhang, ACS Nano **6**, 74 (2012).
[41]W. Dai, H. Dong, B. Fugetsu, Y. Cao, H. Lu, X. Ma, and X. Zhang, Small **11**, 4158 (2015).
[42]M. A. Lukowski, A. S. Daniel, F. Meng, A. Forticaux, L. Li, and S. Jin, J. Am. Chem. Soc. **135**, 10274 (2013).
[43]D. Voiry, H. Yamaguchi, J. Li, R. Silva, D. C. B. Alves, T. Fujita, M. Chen, T. Asefa, V. B. Shenoy, G. Eda, and M. Chhowalla, Nat. Mater. **12**, 850 (2013).
[44]Y.-H. Chang, C.-T. Lin, T.-Y. Chen, C.-L. Hsu, Y.-H. Lee, W. Zhang, K.-H. Wei, and L.-J. Li, Adv. Mater. **25**, 756 (2013).
[45]J. Xie, H. Zhang, S. Li, R. Wang, X. Sun, M. Zhou, J. Zhou, X. W. D. Lou, and Y. Xie, Adv. Mater. **25**, 5807 (2013).
[46]T. Wang, D. Gao, J. Zhuo, Z. Zhu, P. Papakonstantinou, Y. Li, and M. Li, Chem.-Eur. J. **19**, 11939 (2013).
[47]L. G. Bulusheva, V. O. Koroteev, S. G. Stolyarova, A. L. Chuvilin, P. E. Plyusnin, Y. V. Shubin, O. Y. Vilkov, X. Chen, H. Song, and A. V. Okotrub, Electrochim. Acta **283**, 45 (2018).
[48]J. Benson, M. Li, S. Wang, P. Wang, and P. Papakonstantinou, ACS Appl. Mater. Interfaces **7**, 14113 (2015).
[49]G.-Q. Han, X. Li, J. Xue, B. Dong, X. Shang, W.-H. Hu, Y.-R. Liu, J.-Q. Chi, K.-L. Yan, Y.-M. Chai, and C.-G. Liu, Int. J. Hydrogen Energy **42**, 2952 (2017).
[50]G.-Q. Han, X. Shang, S.-S. Lu, B. Dong, X. Li, Y.-R. Liu, W.-H. Hu, J.-B. Zeng, Y.-M. Chai, and C.-G. Liu, Int. J. Hydrogen Energy **42**, 5132 (2017).
[51]D. Yang, M. Chen, S. Wu, D. Zhou, and C. Liu, J. Alloys Compd. **881**, 160593 (2021).
[52]J.-Q. Chi, W.-K. Gao, J.-H. Lin, B. Dong, J.-F. Qin, Z.-Z. Liu, B. Liu, Y.-M. Chai, and C.-G. Liu, J. Catal. **360**, 9 (2018).
[53]B. Guo, J. Sun, X. Hu, Y. Wang, Y. Sun, R. Hu, L. Yu, H. Zhao, and J. Zhu, ACS Appl. Nano Mater. **2**, 40 (2019).
[54]S. Duraisamy, A. Ganguly, P. K. Sharma, J. Benson, J. Davis, and P. Papakonstantinou, ACS Appl. Nano Mater. **4**, 2642 (2021).
[55]D. Strmcnik, P. P. Lopes, B. Genorio, V. R. Stamenkovic, and N. M. Markovic, Nano Energy **29**, 29 (2016).
[56]R. Bar-Ziv, O. E. Meiron, and M. Bar-Sadan, Nanoscale **10**, 16211 (2018).
[57]L. Liu, W.-D. Qu, K.-X. Dong, Y. Qi, W.-T. Gong, G.-L. Ning, and J.-N. Cui, Chem. Commun. **57**, 3339 (2021).
[58]A. P. Murthy, J. Theerthagiri, J. Madhavan, and K. Murugan, Phys. Chem. Chem. Phys. **19**, 1988 (2017).
[59]K. Mensah-Darkwa, R. N. Tabi, M. Owusu, T. Ingsel, P. K. Kahol, and R. K. Gupta, Curr. Graphene Sci. **3**, 11 (2020).
[60]A. Behranginia, M. Asadi, C. Liu, P. Yasaei, B. Kumar, P. Phillips, T. Foroozan, J. C. Waranius, K. Kim, J. Abiade, R. F. Klie, L. A. Curtiss, and A. Salehi-Khojin, Chem. Mater. **28**, 549 (2016).
[61]L. Xu, Y. Zhang, L. Feng, X. Li, Y. Cui, and Q. An, ACS Appl. Mater. Interfaces **13**, 734 (2021).
[62]J. Qin, C. Xi, R. Zhang, T. Liu, P. Zou, D. Wu, Q. Guo, J. Mao, H. Xin, and J. Yang, ACS Catal. **11**, 4486 (2021).
[63]N. Abidi, A. Bonduelle-Skrzypczak, and S. N. Steinmann, J. Phys. Chem. C **125**, 17058 (2021).
[64]S. Gopi, V. Selvamani, and K. Yun, Inorg. Chem. **60**, 10772 (2021).
[65]C. C. L. McCrory *et al.*, J. Am. Chem. Soc. **135**, 16977 (2013).
[66]X. Liu and C. Wang, Catalysts **10**, 1166 (2020).
[67]H. Deng *et al.*, J. Mater. Chem. A **4**, 6824 (2016).
[68]J. Theerthagiri, R. Sudha, K. Premnath, P. Arunachalam, J. Madhavan, and A. M. Al-Mayouf, Int. J. Hydrogen Energy **42**, 13020 (2017).
[69]H. Li, C. Tsai, A. L. Koh, L. Cai, A. W. Contryman, A. H. Fragapane, J. Zhao, H. S. Han, H. C. Manoharan, F. Abild-Pedersen, J. K. Nørskov, and X. Zheng, Nat. Mater. **15**, 364 (2016).
[70]S. Jayabal, G. Saranya, J. Wu, Y. Liu, D. Geng, and X. Meng, J. Mater. Chem. A **5**, 24540 (2017).
[71]X. Zheng, J. Xu, K. Yan, H. Wang, Z. Wang, and S. Yang, Chem. Mater. **26**, 2344 (2014).
[72]J. Zhang, T. Wang, P. Liu, S. Liu, R. Dong, X. Zhuang, M. Chen, and X. Feng, Energy Environ. Sci. **9**, 2789 (2016).
[73]Z. Xing, X. Yang, A. M. Asiri, and X. Sun, ACS Appl. Mater. Interfaces **8**, 14521 (2016).
[74]X. Zou and Y. Zhang, Chem. Soc. Rev. **44**, 5148 (2015).